2020 IEEE/RSJ International Conference on Intelligent Robots and Systems (IROS)
October 25-29, 2020, Las Vegas, NV, USA (Virtual)

Lidar Essential Beam Model for Accurate Width Estimation of Thin Poles

Yunfei Long and Daniel Morris

Abstract— **While Lidar beams are often represented as rays, they actually have finite beam width and this width impacts the measured shape and size of objects in the scene. Here we investigate the effects of beam width on measurements of thin objects such as vertical poles. We propose a model for beam divergence and show how this can explain both object dilation and erosion. We develop a calibration method to estimate beam divergence angle. This calibration method uses one or more vertical poles observed from a Lidar on a moving platform. In addition, we derive an incremental method for using the calibrated beam angle to obtain accurate estimates of thin object diameters, observed from a Lidar on a moving platform. Our method achieves significantly more accurate diameter estimates than is obtained when beam divergence is ignored.**

I. Introduction

Lidar [1], [2] is a widely used active sensor for 3D measurement. Unlike a camera, its measurements are robust to lighting variations including complete darkness. For automated vehicles, Lidar accurately acquires surrounding 3D environments for object detection, recognition and tracking, laying the groundwork for safe autonomous driving in the future. Given its utility and accuracy, it is worth probing the validity of the underlying models used in incorporating Lidar. In particular, Lidar beams are typically approximated as ideal light rays with no width from which 3D point clouds are obtained. Yet in reality, Lidar beams have a finite and diverging width which will impact 3D measurements. This paper investigates these impacts and shows how improved shape accuracy can be obtained by accounting for beam width.

One class of objects impacted by beam divergence are thin rods. Common instances of these are street lamp poles, traffic sign poles, electricity power poles as well as tree trunks. In addition to location, accurate size estimates of such objects are an important part of local scene understanding and contribute towards safe maneuvering. For instance, if an autonomous vehicle needs to navigate through the gap between two poles, precisely sensing both the position and size of the poles may be necessary to safely plan a path between them. Apart from height, the width, i.e. the diameter of a cylinder, determines the size of a thin rod. However, the Lidar is typically not good at accurately measuring such width for two reasons: (1) sparse sampling in azimuth leads to information loss between the samples, and (2) beam divergence may result in sensed Lidar points that extend beyond actual edges (namely width dilation). Such errors distort the measured width of thin objects. For accurate mapping, it would be useful to precisely obtain the width of thin poles from Lidar frames acquired during normal driving. In this paper we show how modeling and estimating beam width is useful for accurate estimation of pole diameters.

When a Lidar beam grazes the edge of an object, whether or not a hit is reported depends not only the spatial energy distribution and the beam's overlap of the object, but also on the internal processing and thresholding mechanism within the Lidar sensor [3]. Rather than selecting our own threshold on beam spread, we prefer to use the Lidar itself to do this based on a series of measurements of pre-defined targets. We call this process Lidar beam calibration, which is introduced in Section IV-C. This motivates us to propose the *essential beam* (EB) as a beam spread model that incorporates both actual energy spread and also internal sensor processing and thresholding of the reflected beam. The EB divergence angle, in conjunction with the azimuth sampling, can be used to make predictions on the number of Lidar samples on thin objects. In turn, these predictions enable us to make precise inferences on the size dimensions of these objects.

The three primary contributions of this paper are:

1) We propose the EB divergence angle to characterize the impact of Lidar beam spread on object boundaries and provide a method to estimate it.
2) Using the EB divergence angle, we determine lower and upper bounds on the number of Lidar samples across the diameter of thin objects.
3) Using the EB divergence angle and number of hits, we estimate lower and upper bounds of thin object diameters. We show that combining these bounds from scans at multiple ranges leads to more accurate diameter estimates than averaging raw measurements.

The consequence of our modeling is that we are able to make more definitive inferences from a Lidar, especially regarding thin objects in a scene.

II. Related work

Lidar is a time-of-flight sensor, acquiring ranges by emitting laser rays and measuring the time light takes to travel to and from objects [2]. To improve measurement performance and explore its limitations, researchers have been studying how the interaction between Lidar beams and environment influences accuracy. Range error models were established [1], [4], taking into account various measurement parameters including range and incidence angle. Additionally, the performance of Lidar has also been tested under different weather and lighting including rain [5], snow,

The authors are with the Department of Electrical and Computer Engineering, Michigan State University, East Lansing, MI 48824, USA {longyunf, dmorris}@msu.edu

978-1-7281-6211-9/20/$31.00 ©2020 IEEE

fog [6], smoke and sunlight [7], [8], which may pose a threat to the safety of self-driving cars. Moreover, researchers have also investigated the impact of object properties on measurement, i.e. shape [8], [2], material [7] and albedo [4]. Lidar is even used to scan specular surface or glass [9] with algorithms developed to reduce undesirable reflections from those surfaces. This paper continues this investigation into Lidar characteristics, but focuses on how the width of diverging laser beams and sparsity of the sampling impact the measurements of width of thin poles, and how to model them to improve accuracy.

The sparse nature of Lidar has been the subject of significant research. Automotive Lidars typically have sparser sampling than cameras, resulting in coarse shape estimates for small or long-range objects. To improve resolution without upgrading to more costly hardware, researchers have developed methods to register multiple frames [10] or combine a Lidar frames with camera images to achieve superresolution [11], [12]. Although missing points between sampling gaps on smooth surfaces can be successfully restored, it remains challenging to precisely recover object boundaries, which is critical for accurate width estimation. Instead of recovering detailed shape of objects, this paper focuses on measuring width of thin poles.

The adverse influence of beam width (namely multi-path effect [13]), often captures people's attention in the most widely-used imaging sensor, the digital camera. It is known that every pixel corresponds to a light ray, whose cross-section area increases with range. A pixel suffers most when its beam region covers high-contrasting surfaces [14]. As a result, the pixel blends intensities. Similar to a camera pixel, a Lidar point corresponds to a laser beam. The range error caused by beam width is widely studied. This error can be large at shape discontinuities such as an object edge when the footprint of a Lidar ray covers both a foreground and a background object before blending the two [1], [4]. It also occurs on surfaces with high-contrasting textures if a ray covers contrasting albedo. A variety of methods have been proposed to identify and remove wrong 3D points due to multi-path effects [15]. However, they focus on beam width's effect on range measurement and this paper highlights its impact on width measurement, which is seldom mentioned in literature. These effects include object dilation and erosion.

The most common model of a Lidar beam width is a cone that linearly diverges with range [1]. The Velodyne 16 Puck Lidar uses such a model with separate horizontal and vertical divergence angles. As the energy of beam spreads out, its boundary may be hard to determine, and the energy of beam cross-section can be modeled as a 2D Gaussian function. Features such as 6σ or full width at half maximum (FWHM) can be used to replace the diameter and compute beam divergence. One way to obtain the the beam divergence angle is to use infrared images of the beam projected on a plane [7] at a known range. However, the precise impact of this beam spread estimate on target hits (i.e. how it decides whether a Lidar point on object boundaries is reflected) is not clear as this depends in addition on internal Lidar processing.

Fig. 1. Our Lidar EB model has a divergence angle, θ, determining a disk with radius, r, which will generate a return if it overlaps an object.

Thus, these models cannot be directly used for accurate width estimation. In contrast to these approaches, our model of beam spread is based on whether a Lidar point is reflected in the real world, and incorporates not only the emitter, but also the Lidar receiver and processor.

To the best of our knowledge, there are no existing methods in the literature specially designed for estimating the width of thin objects using a Lidar. Conventional methods directly estimate horizontal width from the distance of edge points. As we show, this suffers from significant error due to factors such as sparse sampling and finite beam width, which motivates us to propose the EB model which considers these factors. Using this model, we can compensate for beam width and greatly improve measurement accuracy by using multiple Lidar frames collected at different ranges.

III. Lidar Beam Model

Lidar beams diverge with a varying intensity cross section. While various intensity thresholds could determine the width of the beam, here we propose using the *Essential Beam* (EB) model.

Our model for a Lidar EB is a cone, illustrated in Fig. 1 with divergence angle θ and linearly growing radius r. Differing from the full diverging beam, the EB is the "essential" portion that specifies at what radial distance from an object being grazed, the Lidar point will be reflected. That is, the EB radius specifies a disk which, if it overlaps the edge of an object, will generate a return. There is a critical condition when the EB exactly touches the exterior boundary of the object, as shown in Fig. 2 top. In such a scenario, we assume two possible outcomes: the Lidar point is either reflected or not. For brevity, all beams, radius and beam divergence angles mentioned for the rest of this paper refer to EB, EB radius and EB divergence angle, respectively. Note that the cross section of EB needs not be circular, and could be modeled with separate horizontal and vertical EB divergence angle measures, although in this paper we focus purely on the horizontal divergence angle, as this is most relevant to vertical objects.

We assume that horizontal EB radius r increases with range R and the EB divergence angle is expressed as $\theta = 2\arctan(r/R)$. Since θ is small, we approximate it as

$$\theta = \frac{2r}{R}. \tag{1}$$

IV. Object Measurement Model

In this section we explore the measurement consequences of assuming a diverging beam being emitted at discrete azimuth samples by a scanning Lidar

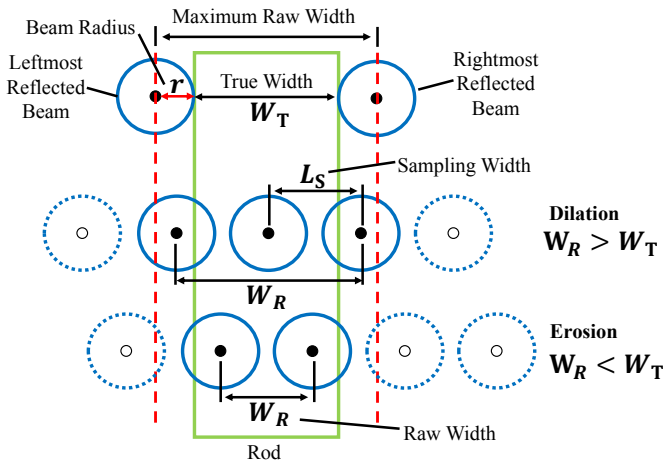

Fig. 2. Diagram of dilation and erosion. The solid rectangle represents a front view of a thin rod with true width W_T. The circles represent cross-sections of EBs and dots at the circle centers are Lidar ray centers, where *solid* dots indicate reflected Lidar rays while *empty* dots at the center of dashed circles are Lidar rays not being reflected. At the top of the figure, we plot two reflected Lidar rays whose EBs exactly touch the exterior boundary of the object. This situation corresponds to the maximum possible dilation, and the maximum dilated object is represented by vertical dashed lines. Thus, the maximum raw width of an object is equal to its true width plus twice the EB radius, r. Below this are two rows of Lidar points with different horizontal positions relative to the object: the middle Lidar row illustrates object dilation, and the bottom row illustrates object erosion.

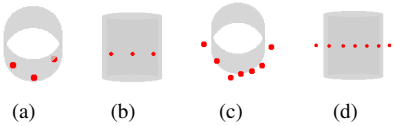

Fig. 3. Examples of object erosion in (a) perspective and (b) front view, and the object dilation in (c) perspective and (d) front view. Both of these effects are explained by our model (shown in Fig. 2) taking into account both azimuth sampling and beam divergence. Each sub-figure shows a row of real Lidar points reflected by a thin rod (shown in Fig. 6(a)). A cylinder with the rod's actual diameter is plotted behind the points for visualization of erosion and dilation.

A. Object dilation and erosion

Erosion and dilation are two types of width measurement consequences of the traditional method. This method estimates horizontal width by finding the distance between the furthest two points reflected by the object along on a row. Given N reflected Lidar points, the estimated width is

$$\hat{W} = (N-1)L_S, \tag{2}$$

where L_S is the sampling length between points. Under the assumption of a thin object, the sampling is uniform and $L_S = \alpha R$, where α is the azimuth sampling angle of the Lidar and R is the average range of points on the row on the object.

We call the width estimated by this traditional method the *raw width*, expressed as W_R. Dilation and erosion are defined by comparing W_R with true width W_T: (1) dilation is when $W_R > W_T$, and (2) erosion is when $W_R < W_T$. These are illustrated in Figs. 2 and 3.

Dilation depends on a finite beam width. The center row of Fig. 2 shows an essential beam overlapping the edge of an object and producing a return. Since the center of the beams are outside the objects, the raw width will be larger than the true width. The maximum dilation on either side of an object is exactly, r, the radius of the EB by definition. This is shown in the top row of Fig. 2.

Erosion is caused by azimuth sampling. The bottom row in Fig. 2 shows erosion since the outermost Lidar points that hit the object are inside the actual boundaries of the object. This results in a smaller raw width than the actual width.

Dilation and erosion are drawbacks of the conventional method for estimating boundaries of objects. This motivates us to propose an object boundary constraint model to compensate for the measurement error.

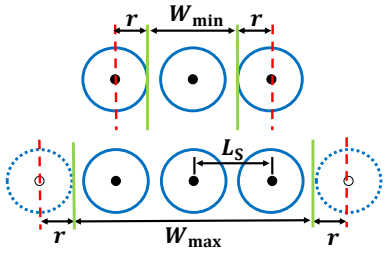

Fig. 4. Given three hits in cross section, $N = 3$, we show two cases: the minimum possible width of the object and the maximum possible width. These are the bounds we derive in Eqs. (4) and (6).

B. Object boundary constraints

The goal of this paper is to combine weak constraints from multiple measurements to obtain a strong or precise constraints on W and θ. Motivated by the occurrence of dilation and erosion, we derive a boundary constraint on θ and the object width W. It is called a boundary constraint because it is derived from two critical situations when there are Lidar rays whose EB exactly touches the exterior boundary of objects. The two situations, illustrated in Fig. 4 top and bottom, corresponds to maximum possible dilation and maximum erosion for a given number of reflected points, respectively.

Assuming that we use a Lidar to scan a vertical pole, of diameter W, at range R and obtain a measurement of N points horizontally across the width of the object, we have the following constraint:

$$(N-1)\alpha \leq \frac{W}{R} + \theta \leq (N+1)\alpha, \tag{3}$$

where θ is EB divergence angle, R is the average range of returned Lidar points (where under the assumption of thin object, the range of all the points within a row are almost identical), and α is the azimuth sampling angle of the Lidar.

Next, Eq. (3) is derived. Consider N adjacent reflected points across an object, illustrated for three points in Fig. 4. Then there are two extreme situations as follows:

(1) The EBs of two boundary points exactly touch object, and are exactly reflected (as shown on top of Fig. 4). This corresponds to the smallest possible width, W_{min}, given N

reflected points, and W_{min} can be expressed as

$$W_{min} = (N-1)L_s - 2r, \tag{4}$$

where L_s is azimuth sampling length and r is EB radius. L_s can be expressed as

$$L_s = \alpha R. \tag{5}$$

The term $(N-1)L_s$ is the distance between two reflected boundary points. Their EBs exactly touch the exterior edge of the rod, as shown in Fig. 4 top, and the width of the rod is $(N-1)L_s - 2r$.

(2) There are two unseen beams whose EB footprints are exactly outside the object (as shown on the bottom of Fig. 4). This situation corresponds to the largest possible width, W_{max}, when there is N reflected horizontal points and W_{max} can be written as

$$W_{max} = (N+1)L_s - 2r, \tag{6}$$

where $(N+1)L_s$ represents the distance between the two unseen points whose EBs of radius r exactly touches the exterior edges of the thin rod. Thus, the width of the rod is $(N+1)L_s - 2r$.

We can express the value range of object width W as

$$W_{min} \leq W \leq W_{max}. \tag{7}$$

After combining Eqs. (1), (4), (5), (6) and (7) we obtain Eq. (3).

C. Calibrating the EB divergence angle θ

Calibration is the process to estimate the EB divergence angle, θ, using a target with known width. Specifically, we estimate θ from multiple scans of a calibration target at different ranges. The target used is a simple thin rod with a uniform diameter of W_T. The procedure is as follows. (1) Place a calibration target (a thin cylinder with a diameter W_T) vertically standing in front of a Lidar. The Lidar records M frames of the target while moving towards or away from the target. (2) For each frame i, count the number of Lidar pixels N_i across the rod diameter and their average range R_i. (3) Then for each frame calculate the bounds, $B_{\theta,i}$, on θ denoted as:

$$(N_i - 1)\alpha - \frac{W_T}{R_i} \leq \theta \leq (N_i + 1)\alpha - \frac{W_T}{R_i}. \tag{8}$$

$B_{\theta,i}$ is obtained by replacing W with the known width W_T, R with R_i and N with N_i in Eqs. (3). A visualization of the upper and lower bounds of θ is shown in Fig. 5(a). Note that in addition, for a real beam, we always have $\theta > 0$.

Combining bounds from multiple frames will shrink the possible range of θ:

$$\theta \in B_{\theta,1} \cap B_{\theta,2} \cap ... \cap B_{\theta,M}. \tag{9}$$

With sufficient samples from various ranges, the lower and upper bounds are likely to converge to the true width. In practice, due to range error and model inaccuracies, some lower bounds may be larger than some upper bounds, making it impossible to directly apply Eq. (9). Thus we estimate $\hat{\theta}$ as the point that best separates the lower bounds from the upper bounds, by finding the global minimum of a convex hinge loss [16].

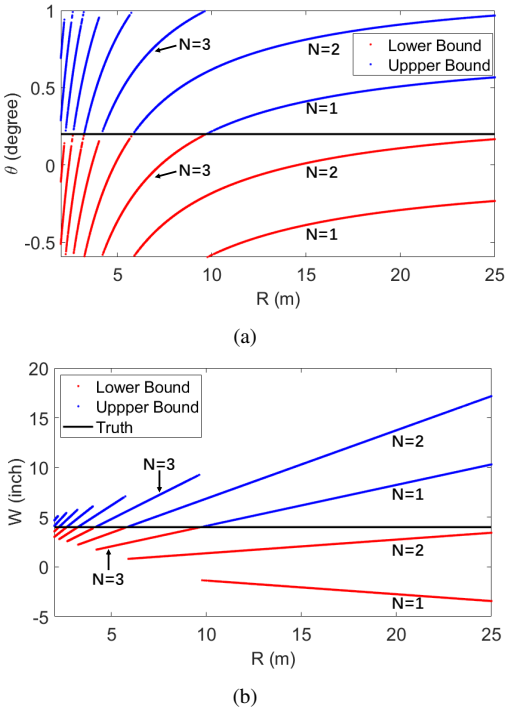

Fig. 5. Visualization of upper bound (in blue) and lower bound (in red) of (a) θ and (b) W, which are expressed in Eqs. (8) and (12), respectively. The actual θ and W is shown in black. The number of points on the bounds are plotted for range R spaced every 0.001 m between 0 and 25 m.

Fig. 5(a) is a visualization of Eq. 8, where θ, α and W_T are set to 0.2 degree, 0.4 degree, and 4 inches, respectively. At a range R_i, we compute a possible N_i. Typically, there are two possible values of N_i, i.e. $\lfloor \frac{W_T+2r}{\alpha R_i} \rfloor$ or $\lfloor \frac{W_T+2r}{\alpha R_i} \rfloor + 1$. In rare cases under critical conditions shown in Fig. 4, there are three possible N_i, i.e. $\frac{W_T+2r}{\alpha R_i} - 1$, $\frac{W_T+2r}{\alpha R_i}$ and $\frac{W_T+2r}{\alpha R_i} + 1$, where $W_T + 2r$ is divisible by αR_i. As mentioned in Section III, the two boundary points whose EBs exactly touch object edge can either be reflected or not. For example, in Fig. 4 top, the possible reflected points can be 1, 2 or 3. At each range, a N_i is randomly selected from all possible values and corresponding upper and lower bounds are plotted according to Eq. (8). It can be seen when N is fixed, the bounds are inversely proportional to range R with a negative sign and some offset. It can also be seen that the upper bounds for N and lower bounds for $N+2$ are on the same curve and they join at the truth. For example, in Fig. 5(a), the upper bound of $N = 1$ connects with the lower bound of $N = 3$ at the true θ. By inserting $N = 1$ and $N = 3$ into right and left part of Eq. (8), respectively, we can express the upper bound of $N = 1$ and lower bound of $N = 3$ as the same function of R, i.e.

$$f(R) = 2\alpha - \frac{W_T}{R}. \tag{10}$$

It is only under the critical condition shown in Fig. 4 (top) that both $N = 1$ and $N = 3$ can be observed for the same

R. Under the critical condition, i.e. EBs of two boundary points exactly touching the object, we have

$$\frac{W_T + 2r}{\alpha R} = 2. \tag{11}$$

Thus, by combining Eqs. (10), (11) and $R = R_C$, where R_C is the range that satisfies the critical condition, we can find that the two bounds are identical at $(R_C, f(R_C))$ where $f(R_C) = \frac{2r}{R_C} = \theta$.

D. Estimating pole width accounting for divergence angle $\hat{\theta}$

As mentioned in Section IV-A, the conventional method computes the width of an object as the distance between two boundary points on an object. This estimate may be significantly biased by erosion or dilation. In our method, using $\hat{\theta}$, we can measure the width of a thin object with high precision. The measurement procedure is the same as that in Section IV-C. With known $\theta = \hat{\theta}$ and unknown W, we can derive bounds for W, i.e. $B_{W,i}$, from Eqs. (3) as

$$\left[(N_i - 1)\alpha - \hat{\theta}\right] R_i \leq W \leq \left[(N_i + 1)\alpha - \hat{\theta}\right] R_i. \tag{12}$$

The visualization of the lower and upper bounds in Eq. (12) is shown in Fig. 5(b). Thus, theoretically, the value of W falls in the overlap region of all the bounds computed from different measurement samples, i.e. N_i and R_i for $i = 1, 2, ..., M$, which as expressed as

$$W \in B_{W,1} \cap B_{W,2} \cap ... \cap B_{W,M}. \tag{13}$$

Similar to Section IV-C, in practice, the estimated width, $\hat{W}$, is computed by minimizing a hinge loss [16] to find the point that best separates the lower bounds from upper bounds.

If a pole width varies over its height, then separate bounds should be calculated at different heights. In the unusual case where width varies with viewing direction, then the bounds can only be combined for measurements from the same viewing directions, such as when directly approaching a pole.

Fig. 5(b) is a plot of the bounds of W at different ranges when $\hat{\theta}$ is set 0.2 deg. Similar to Fig. 5(a), at each range, we randomly pick a possible N_i and plot upper and lower bounds based on Eq. (12). It can be seen when N is fixed, the bounds of W are proportional to R. Similarly, some bounds intersect the truth under critical conditions.

V. Experimental Results

Our experimental setup uses two roof-mounted Lidars, see Fig. 6(a), an Ouster 64 and a Velodyne 16, to scan three white PVC cylinders with diameters of 2, 3 and 4 inches (i.e. 5.08, 7.62 and 10.16 cm), respectively. The azimuth sampling angle α of Ouster and Velodyne are 0.35 and 0.2 degrees, respectively. To collect measurements, we placed one target vertically on a flat ground and drove the vehicle slowly towards it, starting at 30m and ending at 5m from the pole. In each frame, all points on the objects are extracted, and from each row we obtain one measurement i, that consists of the number of horizontal points N_i and their average range R_i.

(a) (b) (c)

Fig. 6. (a) Our EB calibration method uses a scanning Lidar on a moving platform approaching a vertical pole. (b) and (c) are street lamps used for experiments with different materials.

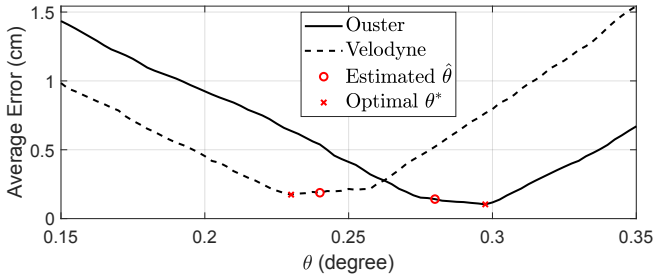

Fig. 7. While we do not know the "true" value for the calibrated EB angle $\hat{\theta}$, we can compare our estimated value with the EB angle that gives the most accurate width estimate for the 3 and 4-inch poles using Eq. (12). We plot the error over possible EB angles θ. This shows that our estimated value is close to the optimal with a very small average diameter error.

A. Calibration of EB and width estimation

To test the validity of our model, we use all the measurements from the 2-inch pole to compute the EB divergence angle θ according to Section IV-C and apply the obtained $\hat{\theta}$ to estimate target width of the 3-inch and 4-inch poles according to Section IV-D, and finally we calculate the average width error of both targets for each Lidar. The estimated EB divergence, $\hat{\theta}$, for Ouster and Velodyne are 0.28 and 0.24 degrees, respectively. We achieve accurate target width estimation, with average error of 0.14 cm and 0.19 cm, both under 0.2 cm, for the Ouster and Velodyne, respectively.

To evaluate the accuracy of the $\hat{\theta}$ obtained via calibration, we investigate how close $\hat{\theta}$ is to the optimal θ^*, the angle that gives the most accurate width prediction via our model. To obtain θ^*, we test a range of angles for θ between .15 and .35 degrees, and compute the resultant width error for the 3 and 4-inch testing poles. The resulting plot of width errors as a function of EB θ are shown in Fig. 7 for the Ouster and Velodyne. From the figure, we can see that our estimates $\hat{\theta}$ are very close to the optimal θ^* values.

B. Comparison with baseline method

To the best of our knowledge, there is no existing method specially designed for estimating the width of thin poles via Lidar. Thus, we adopt the conventional method mentioned in Section IV-A as our baseline method for comparison. It directly computes a raw width by finding the distance between the furthest two reflected points on a row (Eq. (2)). Another method is to accumulate Lidar points, however to avoid smearing this requires maintaining very accurate pose

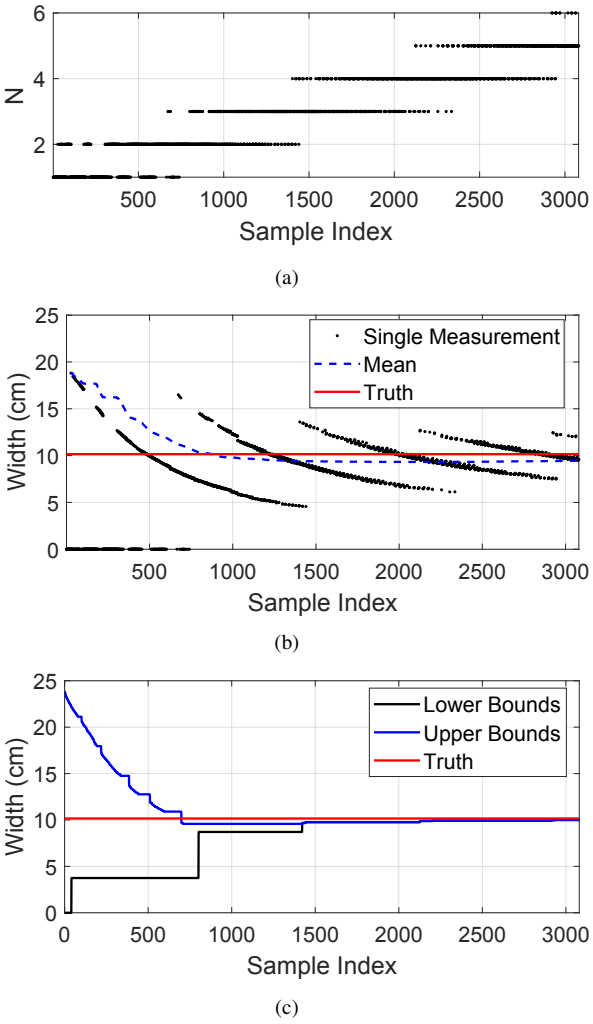

Fig. 8. (a) As the Ouster moves towards a 4-inch rod, we record the number of cross section points, N, at each range R. (b) Our baseline method estimates the pole width (shown in black points) as the distance between maximally separated points for each scan. An incremental average of this is shown in dashed blue. (c) Using $\hat{\theta} = 0.28$, our method computes incremental upper and lower bounds. Initially there is large uncertainty in the pole width, but at around sample 1450 the bounds converge, then the width estimated by hinge loss further approaches the truth.

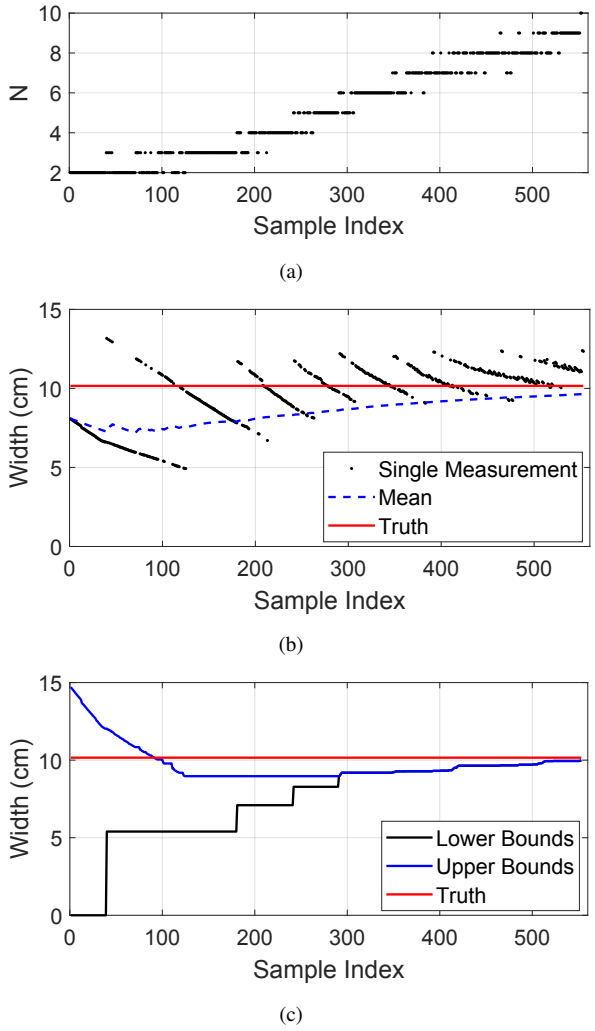

Fig. 9. A repeat of the experiment in Fig. 8, but with the Velodyne approaching a target. (a) The number of pixels in cross section at each sample. (b) The baseline method for estimating a pole width at each sample and its incremental average (dashed blue). (c) Our incremental estimate of bounds as the sensor approaches the target using our calibrated $\hat{\theta} = 0.24$

over an extended time which we do not have, and even this estimate would still suffer from dilation.

We use data from the 4-inch pole to compare our method with the baseline. Each Lidar row at each range contributes a measurement sample of N_i and R_i. The baseline computes the raw width by using Eq. (2) and find the mean over all samples. Our method uses the calibrated EB $\hat{\theta}$ to estimate a width according to Section IV-D. Measurements are accumulated as the vehicle moves towards the pole, and as shown in Figs. 8(a) and 9(a), the number of horizontal reflected points gradually increase as the Lidar moves closer to the object.

The baseline estimates for width are shown in Fig. 8(b) and 9(b). The instantaneous estimates of raw width show significant errors (both larger and smaller than the true width) demonstrating severe dilation and erosion. One extreme case of erosion is that when $N = 1$, the estimated raw width is 0. Note that as the estimation of 0 for $N = 1$ is clearly wrong, we discarded them when computing incremental average estimates. Still, the incremental average estimates are significantly biased. The performance of the mean depends on the overall dilation and erosion of all samples. The mean is biased because it is impractical to collect data in a way that makes the overall dilation exactly compensate for the overall erosion. This shows the need for using our EB divergence angle in estimating widths of thin poles from Lidar samples.

For the proposed method, we draw the upper and lower bounds estimated by Eq. (12) before they converge. Note that bounds shown are accumulated bounds of all previous measurements, and they converge if the lower bound is equal to or greater than the upper bound. After they converge, we plot the width estimated with hinge loss from all obtained bounds. As the Ouster Lidar moves towards the target, the upper and lower bounds on width approach each other and eventually converge close to the truth, as shown in Fig. 8(c).

Although the upper bound goes below the ground truth because of inevitable error, the final hinge-loss-based estimate approaches the truth with more samples. The accumulated lower bound looks like a staircase because the bound only updates when a new lower bound is bigger than current accumulated bound. For example, as shown in Fig. 5(b), when $N = 1$, the lower bounds is smaller than 0. Thus, the lower bound is set to 0 until the first $N = 2$ appears, with a lower bound larger than 0. Because the lower bound of $N = 2$ decreases on approaching the pole, the accumulated lower bound does not change until the first $N = 3$ appears. Similar results for the Velodyne are shown in Fig. 9. For both sensors the proposed method achieves much higher accuracy than the baseline.

The bounds converge under the critical condition when upper bounds and lower bounds join at the truth as shown in Fig. 5(b). Critical condition requires specific ranges as well as specific relative position of Lidar hits on objects as shown in Fig. 5. Because of the randomness of relative positions of Lidar hits on objects in the scanning process, it is uncertain when critical condition is satisfied. Thus, the convergence speed may vary for different driving routes and speeds.

To verify the validity of the proposed model for thin poles with different materials, we use the Ouster to scan two street lamps as shown in Figs. 6(b) and 6(c). The lamp pole is made of stainless steel with a diameter of 17.8 cm and the concrete lamp bases are cylinders with diameters of 47.8 and 60.7 cm, respectively. The true widths are obtained manually with a tape measure. We calibrate θ by using scans of the first lamp and use the second lamp for width measurement.

The EB divergence angle obtained for the stainless steel lamp pole and concrete base are 0.03 and 0.05 degrees, respectively. This dependency of EB divergence angle on material means that dilation and erosion also depend on the interaction between laser beam and specific surface materials as well as internal processing of Lidar. Absolute error of width measurement in comparison with the baseline method is shown in Table I. It is clear that more accurate widths are obtained by the proposed model. This shows that to use of the beam divergence angle, the surface properties of an object need to be identified. We do not address that here, but propose that a classifier could be trained on object reflectivity to identify these properties.

TABLE I

MEASUREMENT ERROR OF THE PROPOSED METHOD AND BASELINE

Objects	Proposed	Baseline
Concrete Base	1.2 cm	8.3 cm
Lamp Pole	1.3 cm	4.1 cm

VI. CONCLUSION

We make the case that there are significant advantages to modeling Lidar beams as diverging rather than as pure rays. Using our proposed EB to characterize this, we can model apparent dilation and erosion of objects, especially thin poles. We provide a calibration method for estimating the EB divergence angle that uses poles of known width in the scene. Using this EB model, we can obtain accurate width estimates for poles, and importantly, identify when we have collected sufficient samples to for obtaining an accurate estimate.

At the moment, our model for EB does not take into account other factors including incident angle, albedo and possible divergence variations with range. In future work, we intend to evaluate how each of these impacts our EB and, if necessary, extend our model to account for them. In addition, we will calibrate a vertical angle for each Lidar.

ACKNOWLEDGEMENTS

This work was supported in part by a gift from Elektrobit.

REFERENCES

[1] M. Hebert and E. Krotkov, "3D measurements from imaging laser radars: how good are they?" *Image and vision computing*, vol. 10, no. 3, pp. 170–178, 1992.

[2] Y. He and S. Chen, "Recent advances in 3D data acquisition and processing by time-of-flight camera," *IEEE Access*, vol. 7, pp. 12 495–12 510, 2019.

[3] J. Laconte, S.-P. Deschênes, M. Labussière, and F. Pomerleau, "Lidar measurement bias estimation via return waveform modelling in a context of 3D mapping," in *IEEE International Conference on Robotics and Automation*, 2019, pp. 8100–8106.

[4] C. Ye and J. Borenstein, "Characterization of a 2D laser scanner for mobile robot obstacle negotiation," in *IEEE International Conference on Robotics and Automation*, vol. 3, 2002, pp. 2512–2518.

[5] C. Goodin, D. Carruth, M. Doude, and C. Hudson, "Predicting the influence of rain on LIDAR in ADAS," *Electronics*, vol. 8, no. 1, p. 89, 2019.

[6] M. Bijelic, T. Gruber, and W. Ritter, "A benchmark for Lidar sensors in fog: Is detection breaking down?" in *IEEE Intelligent Vehicles Symposium*, 2018, pp. 760–767.

[7] F. Pomerleau, A. Breitenmoser, M. Liu, F. Colas, and R. Siegwart, "Noise characterization of depth sensors for surface inspections," in *International Conference on Applied Robotics for the Power Industry*, 2012, pp. 16–21.

[8] Y. He, B. Liang, Y. Zou, J. He, and J. Yang, "Depth errors analysis and correction for time-of-flight (ToF) cameras," *Sensors*, vol. 17, no. 1, p. 92, 2017.

[9] J.-S. Yun and J.-Y. Sim, "Reflection removal for large-scale 3D point clouds," in *IEEE Conference on Computer Vision and Pattern Recognition*, 2018, pp. 4597–4605.

[10] J.-Y. Han, N.-H. Perng, and H.-J. Chen, "LiDAR point cloud registration by image detection technique," *IEEE Geoscience and Remote Sensing Letters*, vol. 10, no. 4, pp. 746–750, 2012.

[11] F. Ma, G. V. Cavalheiro, and S. Karaman, "Self-supervised sparse-to-dense: Self-supervised depth completion from lidar and monocular camera," in *IEEE International Conference on Robotics and Automation*, 2019, pp. 3288–3295.

[12] S. Imran, Y. Long, X. Liu, and D. Morris, "Depth coefficients for depth completion," in *IEEE Conference on Computer Vision and Pattern Recognition*, 2019, pp. 12 438–12 447.

[13] Y. Zhang, D. L. Lau, and Y. Yu, "Causes and corrections for bimodal multi-path scanning with structured light," in *IEEE Conference on Computer Vision and Pattern Recognition*, 2019, pp. 4431–4439.

[14] B. Curless and M. Levoy, "Better optical triangulation through space-time analysis," in *IEEE International Conference on Computer Vision*, 1995, pp. 987–994.

[15] M. Dekan, F. Duchoň, A. Babinec, P. Hubinskỳ, M. Kajan, and M. Szabova, "Versatile approach to probabilistic modeling of Hokuyo UTM-30LX," *IEEE Sensors Journal*, vol. 16, no. 6, pp. 1814–1828, 2015.

[16] P. L. Bartlett and M. H. Wegkamp, "Classification with a reject option using a hinge loss," *Journal of Machine Learning Research*, vol. 9, no. Aug, pp. 1823–1840, 2008.